Environmental Research 263 (2024) 120191

Contents lists available at ScienceDirect

Environmental Research

journal homepage: www.elsevier.com/locate/envres

# Interface engineering of Platinum–Copper alloy/titanium dioxide for enhanced photocatalytic carbon dioxide reduction

Xin Wang [a], Wei Tan [a], Bo Peng [b], Shangcong Sun [b], Xue Li [a], Kaiqiang Wang [c], Jiawei Ji [c], Haohong Liao [c], Jingfang Sun [d], Qing Tong [d], Haiqin Wan [a,*], Lin Dong [a,**]

[a] State Key Laboratory of Pollution Control and Resource Reuse, Jiangsu Key Laboratory of Vehicle Emissions Control, School of Environment, Nanjing University, Nanjing, 210023, PR China
[b] SINOPEC Research Institute of Petroleum Processing Co., Ltd., Beijing, 100083, PR China
[c] State Key Laboratory of Mesoscopic Chemistry of MOE, School of Chemistry and Chemical Engineering, Nanjing University, Nanjing, 210023, PR China
[d] Center of Modern Analysis, Nanjing University, Nanjing, 210023, PR China

ARTICLE INFO

*Keywords:*
Interface structure
PtCu/Ti-$H_2$ catalyst
Hydrogen reduction treatment
Photocatalytic $CO_2$ reduction
$Pt^{\delta+}$-Ov-$Ti^{3+}$
$Cu^{\delta+}$-Ov-$Ti^{3+}$

ABSTRACT

To develop an efficient photocatalytic carbon dioxide ($CO_2$) reduction aimed at mitigating $CO_2$ emissions and greenhouse effects, we propose a straightforward strategy involving hydrogen reduction treatment of PtCu/Ti to create the PtCu/Ti-$H_2$ catalyst with a distinctive interface structure. Compared with the fresh PtCu/Ti catalyst and the benchmark anatase $TiO_2$, the $CH_4$ production of the PtCu/Ti-$H_2$ catalyst increased by 2 times and 81.6 times, respectively. Comprehensive characterizations confirmed the formation of $Pt^{\delta+}$-Ov-$Ti^{3+}$ and $Cu^{\delta+}$-Ov-$Ti^{3+}$ interface structures on the hydrogen-treated PtCu/Ti-$H_2$ catalyst, enhancing light absorption and the separation of photogenerated charge carriers. Further investigation into the reaction mechanism revealed that the $Pt^{\delta+}$-Ov-$Ti^{3+}$ and $Cu^{\delta+}$-Ov-$Ti^{3+}$ species on PtCu/Ti-$H_2$ serve as more favorable sites for $CO_2$ adsorption and activation, promoting an enhanced formaldehyde mechanism. This study not only elucidates the relation between photocatalytic $CO_2$ reduction activity and the PtCu/Ti interface structure but also offers a novel strategy for designing alloy/oxide-based catalysts for $CO_2$ photoreduction, overcoming the limitations of previous studies that focused on metal or vacancy systems.

## 1. Introduction

The rapid and extensive growth of the global population is leading to serious environmental challenges (Khan et al., 2023; Yin et al., 2022), notably the rise in $CO_2$ concentrations from human activities such as fossil fuel combustion, which contribute to global warming and climate change. Artificial photocatalytic systems offer a promising solution by converting $CO_2$ and $H_2O$ into hydrocarbon fuels using solar energy, effectively addressing both global energy demands and climate change concerns (Di et al., 2024; Yoshino et al., 2022; Yu et al., 2023). Among the products of $CO_2$ photoreduction (such as CO, $CH_3OH$, $CH_4$, and various multicarbon compounds), $CH_4$ stands out as a vital clean fuel and an industrial feedstock for the production of carbon black, hydrogen, chloroform, and other high-value chemicals (Gao et al., 2024; Guan et al., 2024; Tang et al., 2022). As a result, achieving a high $CH_4$ yield in $CO_2$ photoreduction has garnered considerable interest. To reach this critical objective, the energy of incoming photons must match or exceed the photocatalyst's bandgap, and the conduction and valence band edges must encompass the potentials for $CO_2$ reduction and $H_2O$ oxidation (Wang et al., 2022b). Therefore, careful selection and design of photocatalysts are essential for this effort.

Various metal-free photocatalysts have been developed for $CO_2$ reduction, including graphitic carbon nitride, elemental phosphorus, boron nitride, and covalent organic frameworks. These photocatalysts utilize non-metallic active sites for the adsorption and activation of $CO_2$ molecules, facilitating the photocatalytic reduction process. For instance, Zhong et al. synthesized a CN-encapsulated melamine–resorcinol–formaldehyde microsphere heterojunction photocatalyst, which effectively adsorbs $CO_2$ to form carbamate species that are selectively photoreduced to methanol. In contrast, metal-based photocatalysts, such as metal oxides and alloys, rely on metal atoms or defect sites on their surface as active sites for $CO_2$ adsorption and activation.

* Corresponding author.
** Corresponding author.
*E-mail addresses:* wanhq@nju.edu.cn (H. Wan), donglin@nju.edu.cn (L. Dong).

https://doi.org/10.1016/j.envres.2024.120191
Received 24 July 2024; Received in revised form 16 October 2024; Accepted 17 October 2024
Available online 18 October 2024

These metal-centered active sites play a critical role in determining the reaction pathway and product selectivity during the photocatalytic reduction of $CO_2$. Xie et al. demonstrated that $CO_2$ adsorbs on Cu active sites within Cu–Ag ASNCs, where the interaction between Cu and Ag enhances $CO_2$ adsorption. Zhou et al. found that $CO_2$ preferentially physically adsorbs on single Au atoms in $Au/CdS_{1-x}$ and is photoreduced to CO, whereas it tends to chemically bond with Cd vacancies in $Au/Cd_{1-x}S$, significantly increasing the rates of CO and $CH_4$ generation. Lin et al. reported that the unsaturated Nb sites in $Nb_2O_{5-x}$ NF materials can anchor $CO_2$ and reduce the desorption of the CO* intermediate, a key factor influencing $CH_4$ selectivity. Therefore, the selection and design of photocatalysts are vital for effective photocatalytic $CO_2$ reduction.

Anatase $TiO_2$ is widely utilized as a photocatalyst for photocatalytic $CO_2$ reduction (Liu et al., 2024) due to its excellent stability, low cost, and high performance. However, $TiO_2$ semiconductors have a relatively large bandgap of approximately 3.2 eV, allowing them to absorb only ultraviolet (UV) light, which constitutes approximately 4% of total sunlight (Imai et al., 2024). This limitation significantly hinders the efficiency of solar energy utilization, resulting in the suboptimal performance of $TiO_2$ as a photocatalyst for photocatalytic $CO_2$ reduction. To enhance $TiO_2$'s photocatalytic activity, researchers have explored the deposition of cocatalysts to expand the light absorption spectrum and increase $CO_2$ adsorption sites (Xie et al., 2024b). Although platinum-based systems exhibit high activity, they are often criticized for their cost and environmental impact. A more effective approach is to alloy transition metals with platinum, reducing the required platinum load. Alloy nanoparticles have gained considerable attention as cocatalysts for photocatalytic $CO_2$ reduction, offering diverse adsorption sites due to their tunable atomic arrangements (Fang et al., 2024). Notably, the PtCu alloy has proven to be an effective cocatalyst for photocatalytic $CO_2$ reduction (Wang et al., 2022a).

Additionally, the interface structure between metals and supports significantly influences catalytic performance (Dong et al., 2024; He et al., 2023; Wang et al., 2024a,b,c; Xie et al., 2024a; Yu et al., 2024). For example, Wang et al. demonstrated that precisely controlling Ir clusters to integrate atomically into the $WO_3$ lattice creates a stable metal-support interface, maximizing the exposure of active metal sites (Wang et al., 2024a,b,c). Dong et al. found that lower-valent Pt atoms at the $CeO_2$ interface, generated by the spontaneous combustion of platinum nitrate, could significantly lower the activation energy of the rate-determining step, thereby enhancing catalytic activity at low temperatures (Dong et al., 2024). Yu et al. reported that the Pt-$CeO_x$ interface, formed by deposing size-controlled Pt nanoparticles on carbon supports coated with ultrathin $CeO_x$ nanosheets, facilitates electron transfer from Pt to $CeO_x$, leading to decreased hydrogen binding energies on Pt surfaces and accelerated water dissociation for the hydrogen evolution reaction (Yu et al., 2024). Among the strategies for regulating interface structure, hydrogen reduction treatment is simple and cost effective, making it a common choice for tuning supported metal catalysts. However, a precise understanding of how atomic structures at alloy/oxide interfaces control catalytic activity remains elusive, and the electron transfer dynamics between alloys and supports at these interfaces are still unclear.

In this study, the interface structure of the PtCu/Ti-$H_2$ catalyst was optimized using a straightforward hydrogen reduction treatment. Through catalytic performance evaluations in photocatalytic $CO_2$ reduction and systematic characterizations, we elucidated a clear structure–performance relationship for the PtCu/Ti-$H_2$ interface structure in this reaction.

## 2. Experimental

Materials: $Pt(acac)_2$ (Pt > 48%) and $Cu(acac)_2$ (98%) were purchased from Alfa Aesar (China) Chemical Co., Ltd. $TiO_2$ (≥99%), oleylamine (80%–90%), and oleic acid (≥99%) were obtained from Shanghai Aladdin Biochemical Technology Co., Ltd., China. $W(CO)_6$ (≥99.8%) was obtained from Tianjin Cines Biochemical Technology Co., Ltd., China. n-Hexane (≥97%) and ethanol (>99.7%) were purchased from Shanghai Peak Chemical Reagent Co., Ltd., China.

### 2.1. Synthesis of PtCu/Ti-$H_2$ catalysts

The preparation of PtCu/Ti was conducted in three steps. First, PtCu alloy nanoparticles were synthesized. Next, these PtCu alloy nanoparticles were dispersed onto anatase-phase $TiO_2$ nanoparticles. Finally, the resulting catalysts underwent hydrogen reduction treatment. The specific steps are as follows.

#### 2.1.1. Synthesis of PtCu alloy nanoparticles

As illustrated in **Scheme 1** of the Supporting Information, PtCu alloy nanoparticles were synthesized using the Schlenk method (Li et al., 2023). Specifically, $Pt(acac)_2$ (0.5 mmol), $Cu(acac)_2$ (0.5 mmol), oleylamine (18.0 mL), and oleic acid (2.0 mL) were added to a three-necked flask, which was then degassed at 25 °C for 1 h under vigorous stirring (typically >500 rpm). The blue-green solution was subsequently heated to 130 °C under an Ar flow. Following this, tungsten hexacarbonyl ($W(CO)_6$, 100 mg) was introduced into the vigorously stirred solution, and the mixture was gradually heated to 240 °C and maintained at that temperature for 40 min. After cooling to room temperature, the resulting mixture was transferred to a 50 mL centrifuge tube and subjected to four rounds of washing and centrifugation with a mixture of n-Hexane and ethanol (in a volumetric ratio of 1:5). The expected product, PtCu alloy nanoparticles, was obtained according to our previous report (Wang et al., 2024a,b,c). Finally, the PtCu alloy nanoparticles were redispersed in n-hexane to form a suspension.

#### 2.1.2. Preparation of PtCu/Ti

PtCu/Ti catalysts were prepared using a modified wetness impregnation method in a rotary evaporator. Anatase-phase $TiO_2$, precalcined at 450 °C for 2 h, served as the support, with the loading of PtCu alloy nanoparticles controlled at 1 *wt*%. After combining the $TiO_2$ support with the nanoparticle suspension into the rotary evaporator, vacuum drying was performed for 8 h to remove n-hexane. The resulting powder was then transferred to a tube furnace for calcination in a 7% $H_2$/Ar atmosphere at 200 °C for 2 h, with a ramp rate of 10 °C·min$^{-1}$. The purpose of the hydrogen calcination was to eliminate surface organic residues. For convenience, the final catalyst was denoted as PtCu/Ti.

#### 2.1.3. Preparation of PtCu/Ti-$H_2$

To regulate the interface structure of the PtCu/Ti catalyst, we subjected it to a direct pretreatment with 7% $H_2$/Ar for an additional 2 h, resulting in the catalyst denoted as PtCu/Ti-$H_2$. Reference catalysts, PtCu/Ti-$H_2$-1h and PtCu/Ti-$H_2$-4h, were prepared similarly, differing only in pretreatment times of 1 h and 4 h, respectively.

To eliminate the influence of surface oxygen vacancies (Ovs) (non-interfacial), we used hydrogen-treated $TiO_2$ as a reference sample, denoted as Ti-$H_2$.

### 2.2. Characterizations

Transmission electron microscopy (TEM) and high-resolution TEM (HRTEM) images were obtained using a JEM-2100 electron microscope operated at an accelerating voltage of 200 kV.

X-ray diffraction (XRD) patterns were obtained using a Philips X'Pert Pro diffractometer with nickel-filtered Cu Kα radiation (λ = 0.15 nm), operating at 40 kV and 40 mA.

$N_2$ adsorption–desorption isotherms were collected at 77 K on a Micrometrics ASAP-2020 adsorption instrument.

Inductively coupled plasma optical emission spectroscopy (ICP-OES) was performed using an Analytik Jena novAA 350/ZEEnit 650 P (Analytik Jena) instrument.

X-ray photoelectron spectroscopy (XPS) analysis was conducted on a PHI5000 Versa Probe high-performance electron spectrometer with monochromatic Al Kα radiation (1486.6 eV). Prior to testing, samples were evacuated in an ultra-high vacuum chamber at room temperature (pressure $<5 \times 10^{-7}$ Pa). The charging effect was mitigated by calibrating all binding energies to the adventitious C 1s peak at 284.6 eV.

UV–vis diffuse reflectance spectroscopy was performed on a Shimadzu UV-2401 spectrophotometer, collecting spectra over a range of 200–800 nm, with $BaSO_4$ as the reference material.

Electron spin resonance (ESR) signals were recorded at 77 K using an ESR JES FA200 spectrometer (JEOL).

Raman spectra were obtained on a LabRAM Aramis spectrometer at an excitation wavelength of 532 nm.

Electrochemical impedance spectroscopy (EIS) and photocurrent testing were conducted with a CHI 660 electrochemical workstation from Shanghai Chenhua Instrument Co., Ltd.

Transient fluorescence spectra were collected on an FLS980 fluorescence spectrophotometer (Edinburgh) with an emission wavelength of 365 nm, using the sample in solid powder form.

A 300-W xenon lamp (CEL-PF300-8) served as a high-power full-spectrum light source, providing a continuous wavelength distribution covering the UV–Vis–IR range from 200 to 1000 nm.

$CO_2$ temperature-programmed desorption ($CO_2$-TPD) experiments were conducted using a multifunctional chemical adsorption analyzer (Tianjin Pengxiang, China). The instrument featured a quartz U-shaped tube reactor, and desorption was monitored with a thermal conductivity detector (TCD). Each sample (100 mg) was pretreated by heating at a ramp rate of 10 °C·min$^{-1}$ under a flow of ultra-high-purity He (30 mL min$^{-1}$) up to 200 °C. After pretreatment, the sample was cooled to room temperature and exposed to a $CO_2$ flow (50 mL min$^{-1}$) through the catalyst bed for 30 min, followed by purging with He (50 mL min$^{-1}$) for 60 min. Subsequently, the sample was heated to 500 °C at a rate of 10 °C·min$^{-1}$, and programmed temperature desorption analysis was performed under a flow of He gas (30 mL min$^{-1}$).

*In situ* diffuse reflectance infrared Fourier transform spectroscopy (DRIFTS) experiments were conducted on a Nicolet 5700 FT-IR spectrometer, equipped with a high-sensitivity mercury cadmium telluride detector cooled by liquid nitrogen. The spectra were collected in the range of 1100–4000 cm$^{-1}$, with a resolution of 4 cm$^{-1}$ (scan number = 32). The *in situ* cell (Harrick) featured a ZnSe window and a temperature control system. Prior to each test, the sample was pretreated with purified Ar gas at 200 °C for 0.5 h to remove any adsorbed impurities from the catalyst. The sample was then cooled to the targeted temperatures. The background spectrum was automatically collected and subtracted from the recorded spectrum. For *in situ* $CO_2$ reduction experiments, a mixture of $CO_2$ and water vapor (generated by bubbling $N_2$) was introduced into the *in situ* cell at a flow rate of 50 mL min$^{-1}$. Spectra were collected every 6 min until adsorption saturation, with a total exposure duration coinciding with 300-W xenon lamp irradiation. For *in situ* CO adsorption experiments, the feeding gas (50 mL min$^{-1}$) consisted of 1% CO (when used), with Ar as the balance gas.

### 2.3. Photocatalytic $CO_2$ reduction experiments

The $CO_2$ photocatalytic reduction reaction was conducted under illumination from a 300 W xenon lamp, using a 100-mL stainless steel high-pressure reactor with a quartz window at the top. The reaction apparatus was equipped with a low-temperature thermostat, allowing for cooling with circulating ethanol (Fig. S1), which helped maintain a constant temperature and reduce experimental error. Error bars were calculated based on the standard deviation from three experimental results. The catalyst (20 mg) was dispersed in 1 mL of $H_2O$, and the resulting suspension was spread on a quartz sand plate. High-purity $CO_2$ (0.2 MPa) was then introduced into the reactor, followed by full-spectrum illumination for 6 h. The generated CO and $CH_4$ were analyzed using a gas chromatograph (GC) equipped with two flame ionization detectors (FIDs) and one TCD. Details of the FID detector for CO and $CH_4$ detection are shown in Fig. S2. In the cycling test, each cycle lasted 6 h, and after each cycle, the used catalysts were washed three times with distilled water and dried in a vacuum oven at 50 °C.

The production of CO and $CH_4$, as well as $CH_4$ selectivity, were calculated using the following equations:

$$P = \frac{A_{sample} C_{standard} PV}{A_{standard} RTm} \quad (1)$$

$$S_{CO} = \frac{2n_{CO}}{2n_{CO} + 8n_{CH4}} \times 100\% \quad (2)$$

where $A_{sample}$ is the peak area for CO/$CH_4$, $A_{standard}$ is the peak area for the CO/$CH_4$ standard area, $C_{standard}$ is the concentration of CO/$CH_4$ standard gas, $P$ is the pressure in the reactor, $V$ is the reactor volume, $R$ is the universal gas constant, $T$ is the reactor temperature, and $m$ is the weight of the catalyst.

## 3. Results and discussion

The chemical compositions of PtCu/Ti and PtCu/Ti-$H_2$ were determined using ICP-OES and XPS (**Table 1**). The results indicated that both the surface and bulk concentrations of Pt and Cu on PtCu/Ti and PtCu/Ti-$H_2$, as obtained from XPS and ICP, closely matched the amounts of Pt and Cu precursors used during synthesis. This suggests that the Pt and Cu species were well-mixed.

XRD patterns of the prepared catalysts were collected to investigate the influence of hydrogen reduction on their crystalline structures. As shown in Fig. S5, all prepared catalysts exhibited characteristic diffraction peaks at 25.3°, 37.8°, 48.0°, 53.9°, 55.1°, 62.7°, 68.8°, 70.3°, and 75.0°, corresponding to the (101), (004), (200), (105), (211), (204), (116), (200), and (215) planes of anatase $TiO_2$ (JCPDS No. 21–1272), indicating that the crystalline structure of the catalysts remained unchanged during hydrogen treatment. No additional peaks corresponding to the PtCu alloy were observed in the PtCu/Ti and PtCu/Ti-$H_2$ catalysts, suggesting that the PtCu alloy was well dispersed on the $TiO_2$ surface without significant aggregation or that its concentration was below the detection limit of XRD (Wang et al., 2023a,b). $N_2$ physisorption experiments were conducted to measure the Brunauer–Emmett–Teller (BET) surface area and explore the pore structure of the catalysts. As shown in Fig. S6a, the adsorption–desorption isotherms of PtCu/Ti and PtCu/-Ti-$H_2$ exhibit H1 hysteresis loops of type IV (as classified by IUPAC) in the relative pressure ($P/P_0$) range of 0.7–1.0, indicating the presence of mesopores (Kruk and Jaroniec, 2001). Notably, the pore diameter of the prereduced catalyst is significantly larger than that of the fresh catalyst, likely due to the removal of organic impurities and the generation of numerous defects during the hydrogen reduction (Fig. S6b)(Xu et al., 2016). The specific surface areas of various PtCu/Ti-*x* catalysts are listed in **Supplementary Table S1**, showing that the prereduced samples exhibit increased specific surface areas, pore volumes, and pore

**Table 1**
Physical properties and chemical compositions of PtCu/Ti and PtCu/Ti-$H_2$ catalysts.

| Sample | Pt content (*wt.*%)[a] | Cu content (*wt.*%)[a] | Pt/Cu (atomic %)[a] | Pt content (atomic %)[b] | Cu content (atomic %)[b] | Particle Size[c] (nm) |
|---|---|---|---|---|---|---|
| PtCu/Ti | 0.76 | 0.25 | 1.00 | 0.39 | 0.41 | 5.1 ± 0.04 |
| PtCu/Ti-$H_2$ | 0.74 | 0.24 | 1.01 | 0.39 | 0.42 | 5.2 ± 0.07 |

[a] Bulk phase concentrations of Pt and Cu were determined using ICP-OES.
[b] Surface atomic concentrations of Pt and Cu were derived from XPS analysis.
[c] The average particle size of PtCu nanoparticles was calculated from particle distribution statistics obtained via TEM.

diameters compared to the fresh PtCu/Ti sample, consistent with the observed pore size profile.

To investigate the morphology of the PtCu/Ti-*x* catalysts, we collected TEM images of the fresh PtCu/Ti and pretreated PtCu/Ti-$H_2$ catalysts. As shown in Fig. 1a and **c**, PtCu nanoparticles in both PtCu/Ti and PtCu/Ti-$H_2$ are uniformly dispersed on the $TiO_2$ support, with similar average particle sizes of approximately 5 nm, indicating no aggregation on the PtCu alloy. Interestingly, HRTEM revealed distinct interface structures for the PtCu/Ti and PtCu/Ti-$H_2$ catalysts (Fig. 1b and d). The PtCu/Ti sample displayed well-defined PtCu nanoparticles with characteristic lattice fringes corresponding to the PtCu alloy (0.21 nm), along with clear boundaries on the $TiO_2$ support (Chen et al., 2020). In contrast, the prereduced PtCu/Ti-$H_2$ sample exhibited a blurred boundary between the PtCu alloy and the $TiO_2$ support, suggesting that the interface structure has changed as a result of the hydrogen reduction treatment.

To investigate the electronic state of Pt species, we conducted *in situ* DRIFTS of CO adsorption at 25 °C. As shown in Fig. 2a and b, a clear difference in CO adsorption between PtCu/Ti and PtCu/Ti-$H_2$ is observed. Both samples exhibit bands of approximately 2020 $cm^{-1}$ corresponding to CO adsorption on metallic Pt species ($Pt^0$) (Liu et al., 2021). However, a new intense band appears at 2051 $cm^{-1}$ for PtCu/-Ti-$H_2$, which is assigned to linear CO adsorption on positively charged Pt species ($Pt^{\delta+}$) at the interfacial site (Zhou et al., 2016). The wavenumbers of both bands are lower than those of the corresponding bands, likely due to the alloy effect. These observations indicate that the predominant Pt species in PtCu/Ti is $Pt^0$, whereas both $Pt^0$ and $Pt^{\delta+}$ species coexist in PtCu/Ti-$H_2$, with $Pt^{\delta+}$ originating from the interface.

To investigate the electron transfer between the PtCu alloy and $TiO_2$ after hydrogen reduction treatment, we analyzed the electronic properties of PtCu/Ti and PtCu/Ti-$H_2$ using XPS. From the Cu $2p_{3/2}$ and Pt $4f_{7/2}$ XPS (Fig. 2c and d), it can be concluded that Cu and Pt in PtCu/Ti and PtCu/Ti-$H_2$ predominantly exist as $Cu^0$ and $Pt^0$ species (Lee et al., 2016). Following hydrogen reduction at 200 °C, the binding energies for Cu $2p_{3/2}$ and Pt $4f_{7/2}$ shifted from 931.0 to 931.4 eV and from 70.3 to 70.4 eV, respectively, indicating that Cu and Pt lose electrons during the treatment, suggesting the potential formation of $Cu^{\delta+}$ and $Pt^{\delta+}$ species. Furthermore, as shown in Fig. S7, no significant signal was detected in the W 4f XPS region (32–40 eV), confirming the absence of tungsten in the sample. The ratios of surface $Ti^{3+}$ and $O_{ads}$ species across all catalysts are presented in Fig. 3a and b to illustrate the electron transfer after hydrogen reduction. Compared to Ti, the concentrations of surface $Ti^{3+}$ and $O_{ads}$ species on Ti-$H_2$ increased to 5.6% and 30.8%, respectively, due to $H_2$ dissociation and Ov formation (Nakamura et al., 2011). After PtCu deposition on $TiO_2$, the concentration of surface $Ti^{3+}$ increased, while $O_{ads}$ concentration decreased, indicating that partial surface Ovs were covered by PtCu nanoparticles and replenished by $O_2$. After hydrogen reduction treatment, the surface concentrations of $Ti^{3+}$ and Ovs in the PtCu/Ti-$H_2$ sample significantly increased, accompanied by a shift in Ti 2p to lower binding energies, illustrating that Ti gains electrons during reduction. Combined with the Cu $2p_{3/2}$ and Pt $4f_{7/2}$ XPS results, this confirms that hydrogen reduction facilitates electron transfer from Pt and Cu to Ti. Notably, the higher concentrations of $Ti^{3+}$ and Ovs in the PtCu/Ti-$H_2$ sample compared to the Ti-$H_2$ sample imply the presence of more Ovs at the PtCu/Ti-$H_2$ interface. Overall, the combined CO-DRIFTS and XPS results suggest that abundant $Pt^{\delta+}$-Ov-$Ti^{3+}$ and $Cu^{\delta+}$-Ov-$Ti^{3+}$ species are formed at the interface of PtCu/Ti-$H_2$ after the reduction treatment (Liu et al., 2021).

To further confirm the electron transfer during the $H_2$ reduction treatment, we examined the presence of Ovs and $Ti^{3+}$ species using sensitive electron paramagnetic resonance (EPR) measurements (Howe and Gratzel, 1985). As shown in Fig. 4a, the EPR spectra of Ti-$H_2$,

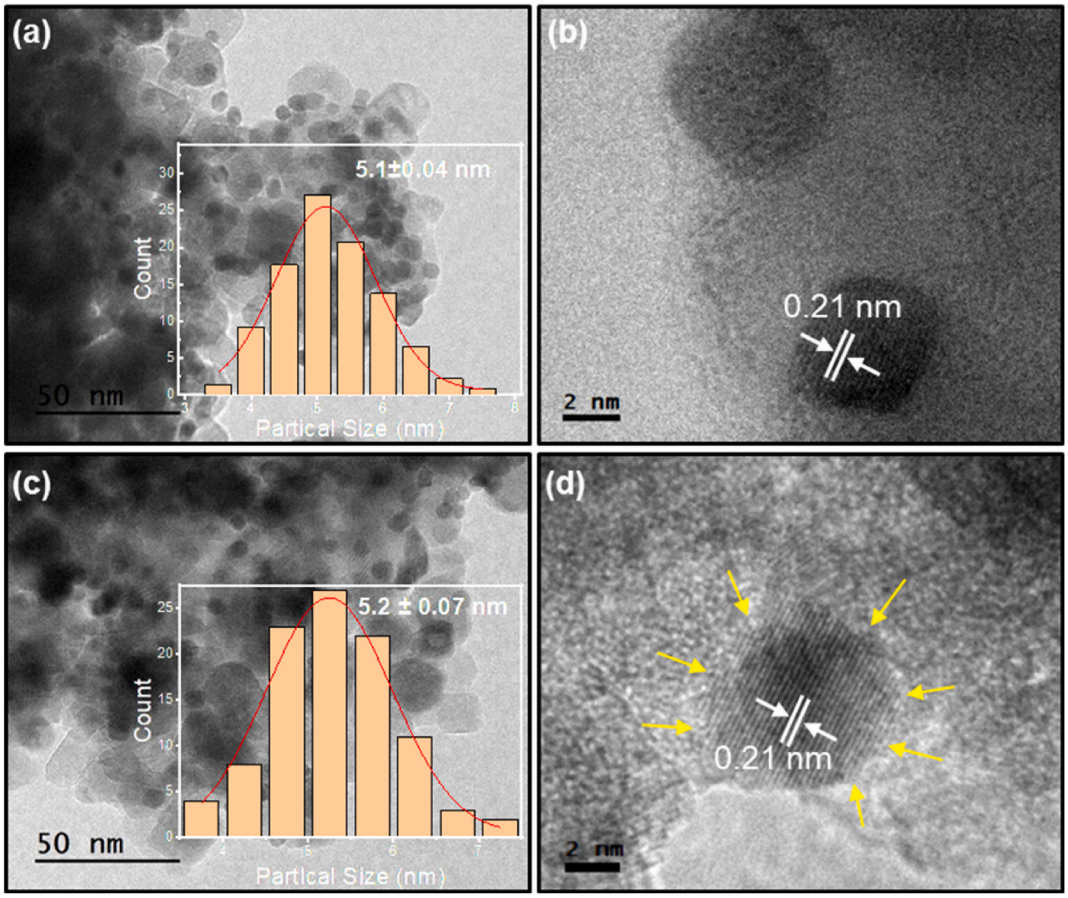


**Fig. 1.** TEM images of fresh PtCu/Ti (a, b) and pretreated PtCu/Ti-$H_2$ (c, d) catalysts.

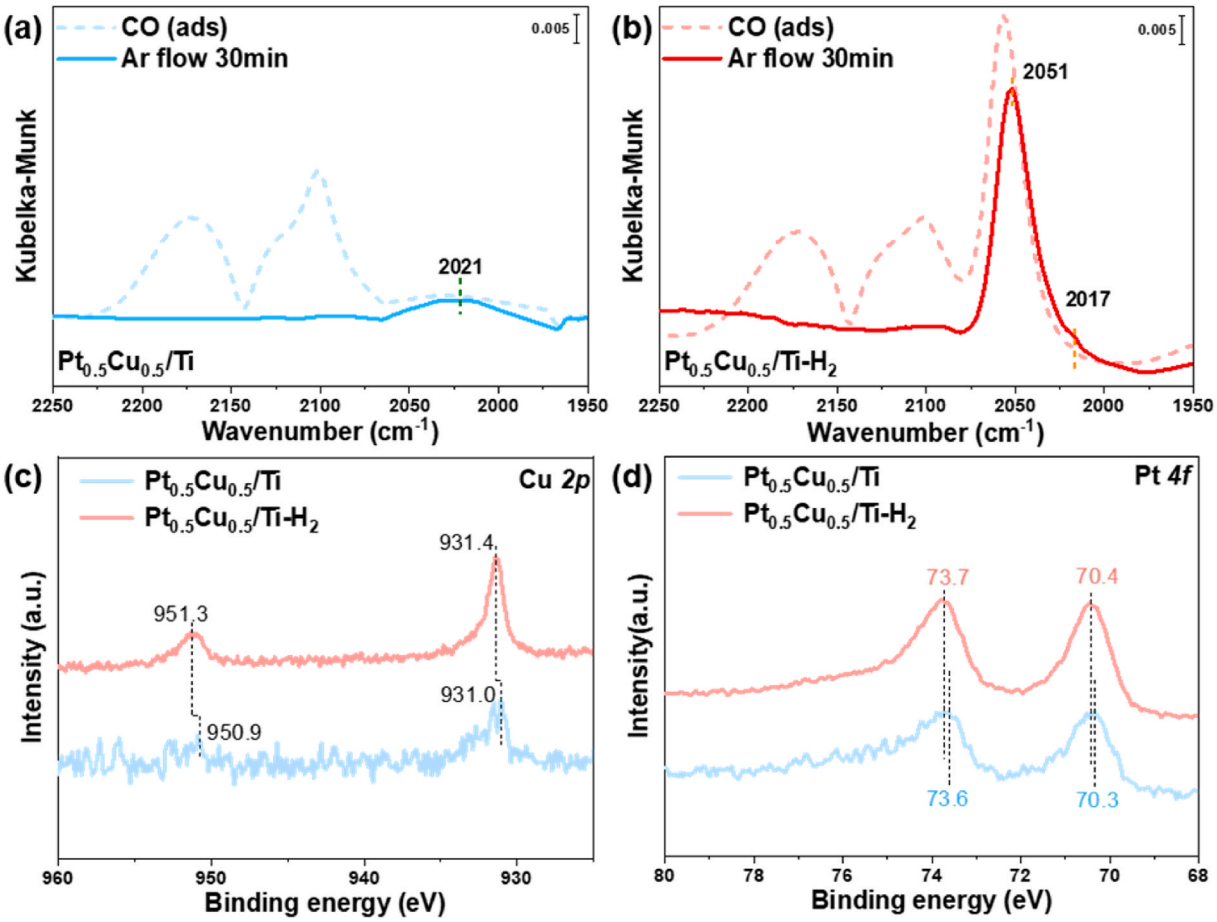


**Fig. 2.** *In situ* DRIFTS of CO adsorption on fresh PtCu/Ti (a) and pretreated PtCu/Ti-$H_2$ (b); XPS of Cu 2p (c) and Pt 4f (d) for both fresh PtCu/Ti and pretreated PtCu/Ti-$H_2$.

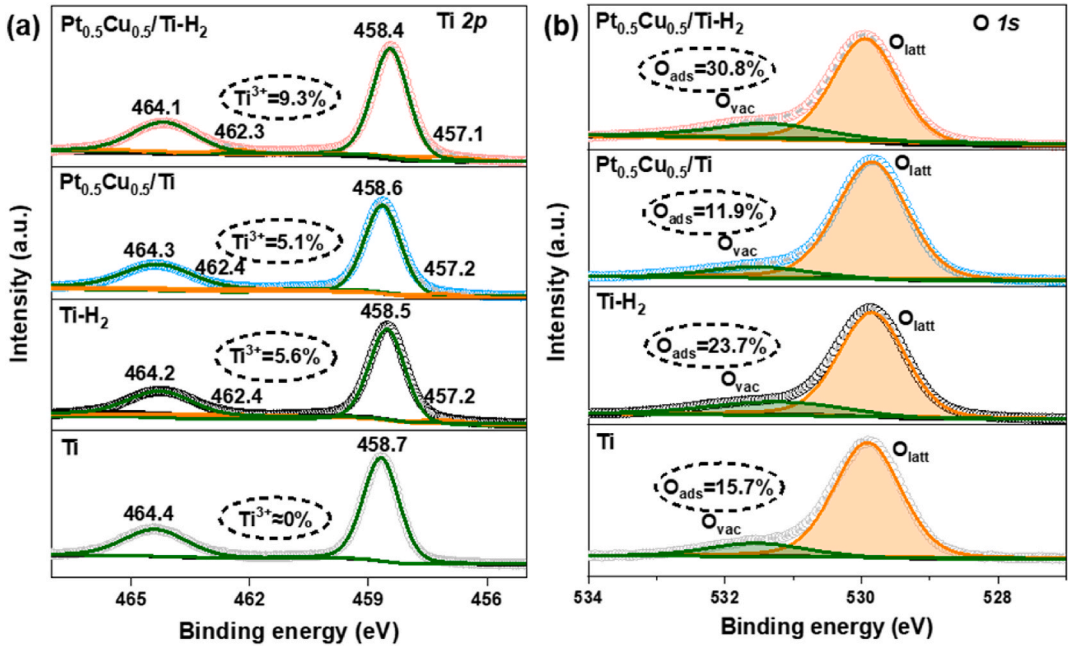


**Fig. 3.** XPS spectra of Ti 2p (a) and O 1s (b) for fresh PtCu/Ti and pretreated PtCu/Ti-$H_2$.

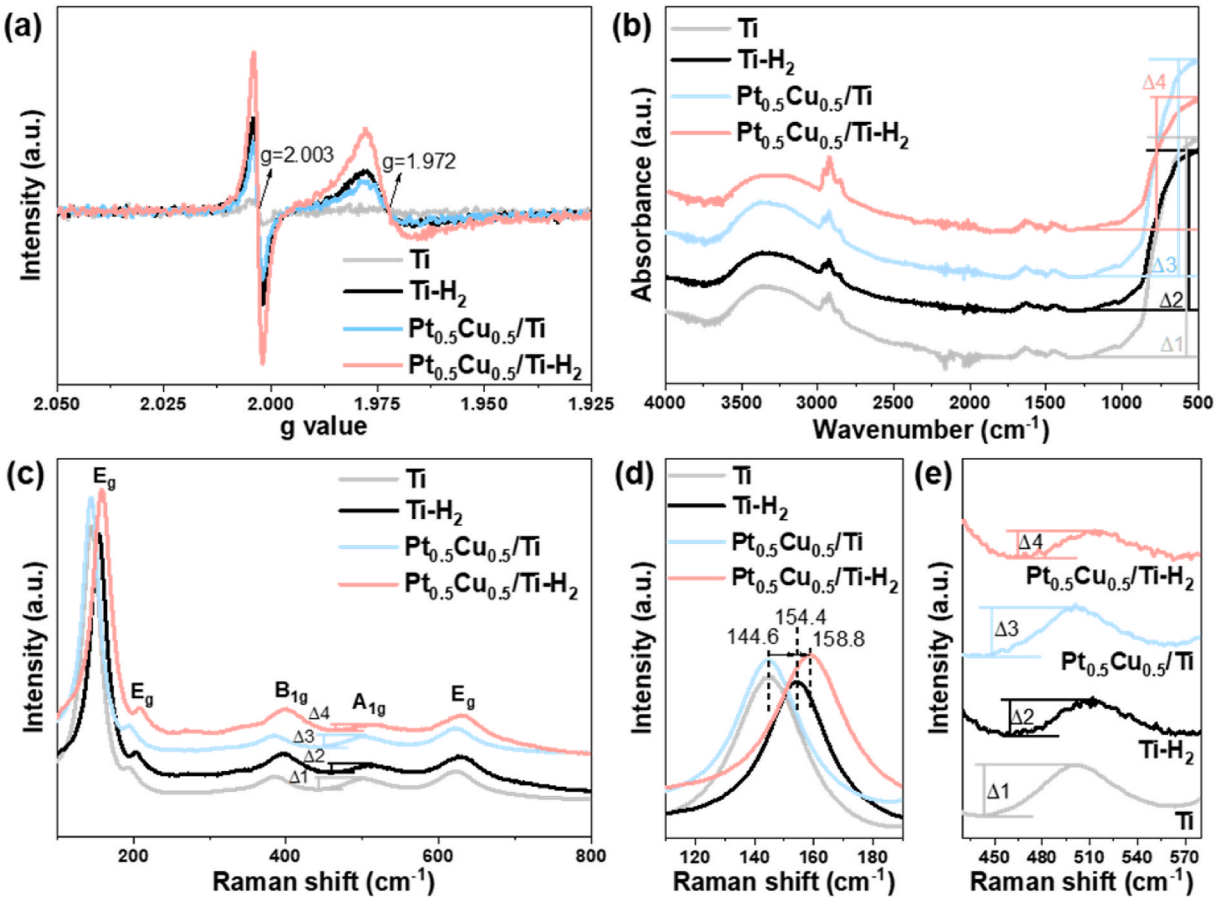


**Fig. 4.** Surface structure of fresh Ti, pretreated Ti-$H_2$, fresh PtCu/Ti, and pretreated PtCu/Ti-$H_2$; (a) ESR results; (b) ATR-FTIR spectra; (c), (d), and (e) Raman spectra.

PtCu/Ti, and PtCu/Ti-$H_2$ reveal signals at g = 2.003 and g = 1.975, which are attributed to Ov and $Ti^{3+}$ defects, respectively. In the fresh Ti sample, no signal corresponding to $Ti^{3+}$ was observed; however, a weak signal for Ov was detected, consistent with the Ti 2p XPS results and indicating a small number of reduced $TiO_x$ species in the Ti sample. In contrast, PtCu/Ti-$H_2$ shows a significant increase in the intensity of both Ov and $Ti^{3+}$ signals compared to Ti and Ti-$H_2$. This enhancement aligns with the XPS results, suggesting that PtCu alloy promotes the generation of Ov and $Ti^{3+}$ defect species at the interface between the PtCu alloy and the $TiO_2$ support, alongside the transfer of electrons from Pt and Cu to Ti.

Fourier transform infrared spectroscopy (FTIR) analysis provided insights into the functional groups, molecular geometry, and intra- or inter-molecular interactions within the samples. Attenuated total reflectance FTIR (ATR-FTIR) spectra were collected to assess the changes in the interface structure following the $H_2$ reduction treatment. As shown in Fig. 4b, the band at 530 $cm^{-1}$ corresponds to the vibration of the Ti–O–Ti bond (Ruiz Santoyo et al., 2021). The normalized intensity of this band follows the sequence: PtCu/Ti-$H_2$ (Δ4) < Ti-$H_2$ (Δ2) < PtCu/Ti (Δ3) ≈ Ti (Δ1). This indicates a partial breaking of the surface Ti–O–Ti bonds due to the hydrogen reduction treatment, which results in the generation of Ovs at the interface and surface. Notably, PtCu/-Ti-$H_2$ demonstrates a higher concentration of Ov defects compared to Ti-$H_2$, highlighting the influence of the PtCu/Ti-$H_2$ interface.

To further validate this speculation, Raman spectra were collected for all samples (Fig. 4c). Characteristic Raman vibration peaks of anatase $TiO_2$ were observed, including the $E_g$ modes at 144 $cm^{-1}$, 198 $cm^{-1}$, and 638 $cm^{-1}$, as well as $B1_g$ (398 $cm^{-1}$) and $A1_g$ (520 $cm^{-1}$) modes (Wang et al., 2021). The band at ~144 $cm^{-1}$ is attributed to the $E_g$ mode, which is influenced by defects in the anatase $TiO_2$ structure. An enlarged view of the region from 110 to 190 $cm^{-1}$ (Fig. 4d) reveals that the $E_g$ band position of $TiO_2$ after hydrogen reduction shifts from 144.6 to 154.4 $cm^{-1}$, indicating the generation of numerous Ovs on the sample surface due to reduction treatment (Janotti et al., 2010). The $E_g$ mode band position for PtCu/Ti (144.8 $cm^{-1}$) shows no significant difference compared to that of the fresh $TiO_2$ support (144.6 $cm^{-1}$), suggesting negligible interaction between the $TiO_2$ support and the PtCu alloy. Interestingly, the Eg band of the PtCu/Ti-$H_2$ sample after hydrogen reduction shifts to a higher wavenumber of 158.8 $cm^{-1}$. This shift is attributed to the interaction between the PtCu alloy and $TiO_2$ resulting from the hydrogen reduction treatment, which leads to an increased generation of Ovs at the interface between the PtCu alloy and $TiO_2$. This finding is further supported by the ATR spectra. Additionally, the intensity sequence of the $A1_g$ band, associated with Ti–O bonds, follows the order: PtCu/Ti-$H_2$ (Δ4) < Ti-$H_2$ (Δ2) < PtCu/Ti (Δ3) ≈ Ti (Δ1) (Fig. 4e). This sequence is consistent with the intensity of the Ti–O–Ti bonds observed in the ATR spectra, reinforcing the conclusion that more surface Ovs are present at the PtCu/Ti-$H_2$ interface. In summary, the results from CO-DRIFTS, XPS, EPR, ATR-FTIR, and Raman spectra collectively confirm the formation of significant amounts of $Pt^{\delta+}$-Ov-$Ti^{3+}$ and $Cu^{\delta+}$-Ov-$Ti^{3+}$ interface structures in PtCu/Ti-$H_2$.

The catalytic performance of the prepared samples was evaluated for photocatalytic $CO_2$ reduction. First, we investigated the effects of several parameters, such as $CO_2$ concentration, $CO_2$ pressure, temperature, and catalyst dosage, on the activity of the PtCu/Ti-$H_2$ sample. As shown in Fig. S12, both $CH_4$ yield and selectivity increased with higher $CO_2$ concentrations. Notably, the PtCu/Ti-$H_2$ catalyst maintained high $CO_2$ reduction performance even at lower concentrations, indicating its potential for practical applications. $CH_4$ yield also increased with rising $CO_2$ pressure (Fig. S13); however, excessively high pressures may hinder large-scale applications. Fig. S14 illustrates that as the temperature

increased, the yield of CO significantly increased, accompanied by more $H_2$ production. This indicates that temperature affects product distribution in the photocatalytic $CO_2$ reduction process. Higher temperatures promote the formation and desorption of products such as $H_2$ and CO, while lower temperatures favor the hydrogenation of *CO to produce $CH_4$. As shown in Fig. S15, catalyst activity increased with the amount of catalyst used. However, the mass-normalized $CH_4$ yield with 50 mg of catalyst was significantly lower than that with 20 mg, as the catalyst amount exceeded the illuminated area of the reactor. Based on these tests, the optimized conditions for photocatalytic $CO_2$ reduction were determined to be 0.2 MPa $CO_2$, 1 mL $H_2O$, and 20 mg of catalyst over 6 h. Fig. 5a reveals that the fresh Ti sample exhibited limited activity, yielding 4.2 μmol $g^{-1}$ of $CH_4$ and 1.6 μmol $g^{-1}$ of CO. Consistent with previous reports (Shen et al., 2021), pretreatment of Ti-$H_2$ resulted in a moderate increase in $CH_4$ and CO production, primarily due to the enhanced surface Ovs that facilitate $CO_2$ adsorption. The deposition of a PtCu alloy on the $TiO_2$ surface significantly improved $CO_2$ reduction efficiency, achieving $CH_4$ and CO yields of 48.0 and 34.0 μmol $g^{-1}$, respectively. Notably, pretreatment of fresh PtCu/Ti led to further enhanced activity in PtCu/Ti-$H_2$ samples, with $CH_4$ yields 33.6 times and 2 times higher than those of Ti-$H_2$ and PtCu/Ti, respectively. This indicates that the $Pt^{\delta+}$-Ov-$Ti^{3+}$ and $Cu^{\delta+}$-Ov-$Ti^{3+}$ interface structures facilitate the photocatalytic reduction of $CO_2$ to $CH_4$. Although the BET surface area of PtCu/Ti-$H_2$ increased slightly after hydrogen treatment, this change alone cannot account for the substantial enhancement in catalytic performance. The markedly higher activity of PtCu/Ti-$H_2$ compared to Pt/Ti-$H_2$ and Cu/Ti-$H_2$ further confirms the synergistic effect between Pt and Cu in the PtCu alloy, consistent with our previous work. To facilitate a straightforward comparison of catalytic performances, we normalized the $CH_4$ yields of different photocatalysts based on noble metal content per millimole. As shown in column 5 of **Supplementary Table S2**, PtCu/Ti-$H_2$ exhibited excellent performance among these noble metal–based catalysts. We also investigated the stability of PtCu/Ti-$H_2$ under reaction conditions through long-term activity tests. As shown in Fig. 5b, PtCu/Ti-$H_2$ continuously produced $CH_4$ and CO under UV–vis light irradiation for up to 24 h. After eleven cycles, PtCu/Ti-$H_2$ maintained excellent photocatalytic $CO_2$ reduction activity, indicating outstanding stability (Fig. S16). The catalyst was characterized by post-photocatalytic $CO_2$ reduction to assess its structural stability. XRD results (Fig. S17) indicate that the crystal structure of the catalysts remained unchanged after photocatalysis. XPS analysis explored the chemical states of surface elements, revealing that Cu and Pt in the used catalysts remained in their metallic states after $CO_2$ reduction testing (Fig. S18). Notably, the contents of $Ti^{3+}$ and $O_{ads}$ in the used PtCu/Ti catalyst decreased significantly after photocatalytic $CO_2$ reduction (Fig. S19), whereas these values remained nearly unchanged for PtCu/Ti-$H_2$. This decrease in $Ti^{3+}$ and $O_{ads}$ content suggests greater consumption of Ovs during catalysis, likely due to strong adsorption of intermediates and catalyst poisoning/deactivation. However, the more favorable $Pt^{\delta+}$-Ov-$Ti^{3+}$ and $Cu^{\delta+}$-Ov-$Ti^{3+}$ interfacial structures for activating intermediate species contribute to better stability of PtCu/-Ti-$H_2$. To further examine the stability and the density of Ovs on the catalyst surface throughout the reaction, EPR tests under real reaction conditions (in a $CO_2$ atmosphere) and post-photocatalytic $CO_2$ reduction were conducted. As shown in Fig. S20, Ov and $Ti^{3+}$ content significantly decreased under reaction conditions, indicating $CO_2$ adsorption at these

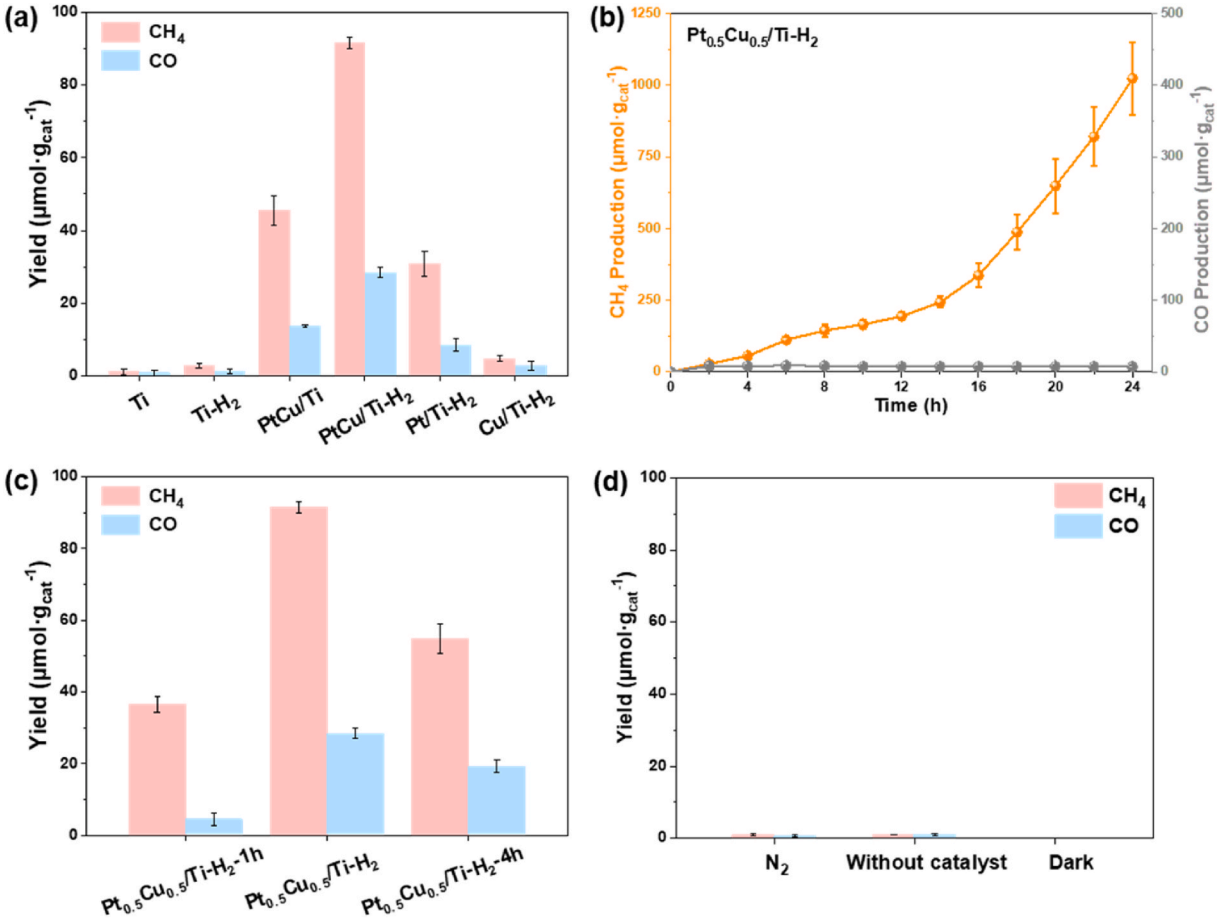


**Fig. 5.** Performance evaluation of photocatalytic $CO_2$ reduction; (a) all samples; (b) stability of the PtCu/Ti-$H_2$ catalyst; (c) PtCu/Ti catalysts with varying hydrogen pretreatment durations; (d) control experiment under $N_2$ conditions, without catalyst and light. (Reaction conditions: 0.2 MPa of $CO_2$, 1 mL of $H_2O$, and 20 mg of catalyst for 6 h).

sites. Interestingly, the Ov content on the catalyst surface post-reaction was nearly identical to that before the reaction, suggesting that reaction intermediates effectively desorb from the Ovs without causing catalyst deactivation. This result aligns with the XPS findings before and after photocatalytic $CO_2$ reduction. Moreover, no $H_2$ was detected during the photocatalytic reaction, implying that $CO_2$ reduction selectivity is higher than that for $H_2O$ reduction or that H atoms from $H_2O$ serve as hydrogen sources for $CH_4$ production (Fig. S21). External quantum efficiency (EQE) is a critical intrinsic parameter for evaluating the photon-to-product efficiency of a photocatalytic system. Thus, EQE values for PtCu/Ti-$H_2$ and PtCu/Ti-$H_2$ were tested. As shown in **Supplementary Table S4**, the EQE values for $CH_4$ production using PtCu/Ti-$H_2$ were 0.366%, 0.089%, 0.063%, and 0.048% at wavelengths of 325 nm, 420 nm, 450 nm, and 475 nm, demonstrating comparability to natural photosynthesis (Du et al., 2024). Conversely, PtCu/Ti exhibited a notably lower $CH_4$ production rate at the same wavelengths (**Supplementary Table S3**) and lower EQE values of 0.105%, 0.0011%, 0.00058%, and 0.00045%, indicating inferior performance relative to PtCu/Ti-$H_2$. To investigate the role of interactions in photocatalytic $CO_2$ reduction, we subjected samples to hydrogen reduction treatment for varying durations and tested their reaction activities. As shown in Fig. 5c, $CH_4$ and CO production initially increased with longer hydrogen reduction time before decreasing. The PtCu/Ti-$H_2$ sample treated with hydrogen for 2 h exhibited the highest reaction activity. To further explore this phenomenon, ATR-FTIR analysis of PtCu/Ti-$H_2$-1h was conducted. As shown in Fig. S22, the surface of PtCu/Ti-$H_2$-1h displayed three bands attributed to N=H, C=O, and C–H, suggesting partial coverage of PtCu nanoparticles by organic species such as oleylamine. This observation is consistent with BET analysis results, indicating that residual organic species on nanoparticle surfaces led to lower reactivity compared to PtCu/Ti-$H_2$. In contrast, prolonged hydrogen reduction treatment resulted in stronger interactions between the PtCu alloy and $TiO_2$, which did not facilitate photocatalytic $CO_2$ reduction. This indicates that appropriate interactions are more favorable for $CH_4$ and CO production. Photocatalytic $CO_2$ reduction activity was also tested under conditions of $N_2$, without a catalyst, and without light. As shown in Fig. 5d, almost no $CH_4$ and CO were produced, confirming that all the $CH_4$ and CO generated in the system originated from $CO_2$ reduction. To explore all potential products, we conducted $^{13}C$ tracing GC–mass spectrometry tests using $^{13}CO_2$ as the carbon source. The $m/z$ values detected in the $^{13}C$ tracing experiments were 17 ($^{13}CH_4$) and 29 ($^{13}CO$), confirming that the carbon-containing products in the system were $CH_4$ and CO, both derived entirely from $CO_2$ reduction.

Point zero charge (PZC) is a crucial parameter for evaluating the surface adsorption strength of an adsorbent (Putri et al., 2024). As shown in Fig. S23, the PZC values for PtCu/Ti and PtCu/Ti-$H_2$ are 7.92 and 5.01, respectively. Consequently, PtCu/Ti experienced electrostatic repulsion from positively charged $H^+$ cations at experimental conditions (pH = 7), while PtCu/Ti-$H_2$ electrostatically adsorbed $H^+$. This difference explains why PtCu/Ti-$H_2$ exhibited stronger hydrogenation ability.

To investigate the photoelectrical properties of the catalysts, we conducted photocurrent response tests, with the results presented in Fig. 6a. The photocurrent response followed the order: PtCu/Ti-$H_2$ > PtCu/Ti > Ti-$H_2$ > Ti. This trend is attributed to the significant role of Ovs in influencing charge carrier behavior, particularly based on their location. Ov at the interface typically exhibits higher stability, facilitating the separation of photoinduced electron–hole pairs. Supporting this, the EIS results in Fig. 6b show that Ti has the largest arc radius in the EIS curve, indicating the highest impedance value. After the hydrogen reduction treatment, the arc radius for the Ti-$H_2$ sample

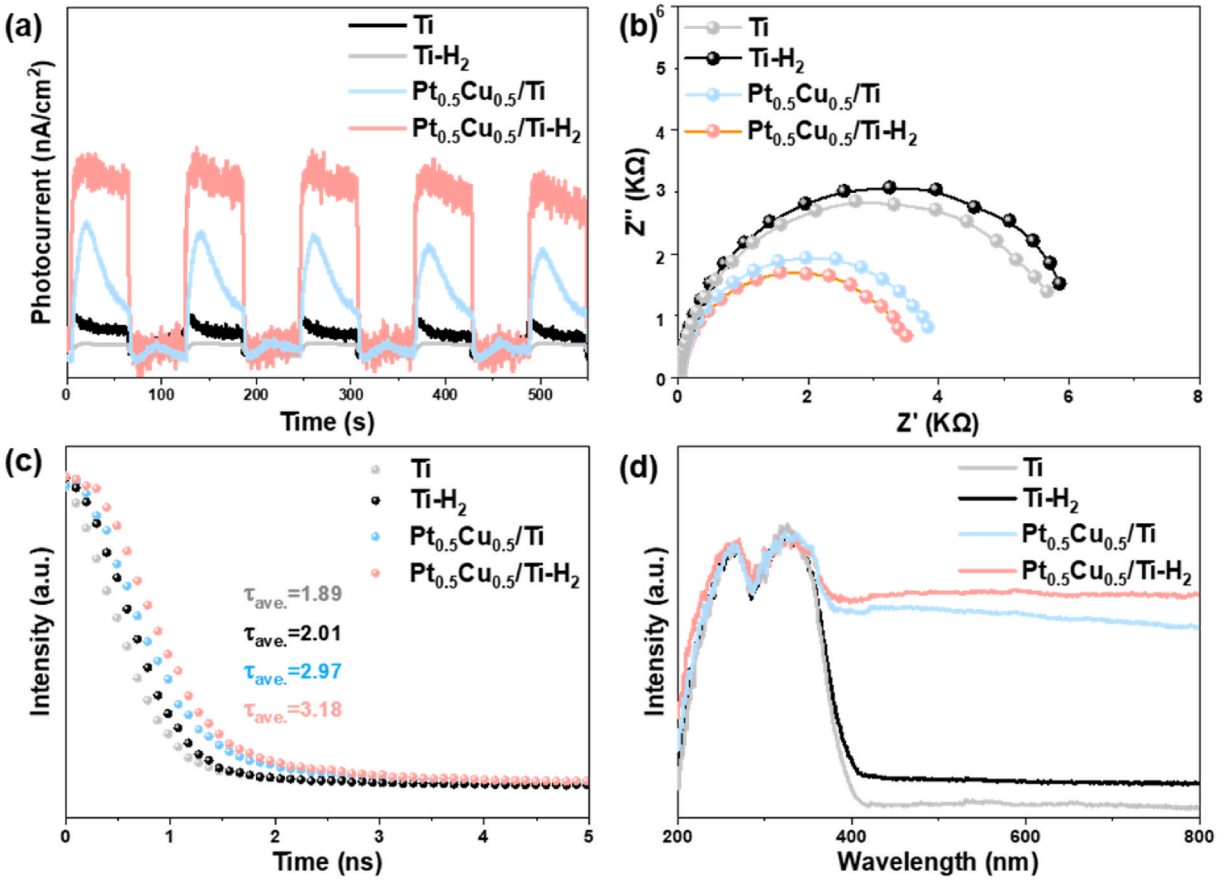


**Fig. 6.** Photoelectronic test results for fresh Ti, pretreated Ti-$H_2$, fresh PtCu/Ti, and pretreated PtCu/Ti-$H_2$; (a) photocurrent responses; (b) EIS curves; (c) time-resolved photoluminescence spectra; (d) UV–vis spectra.

decreases slightly. In contrast, PtCu/Ti-$H_2$ displays the smallest arc radius, significantly lower than that of the hydrogen-treated Ti-$H_2$ sample, demonstrating that interface Ov enhances the separation of photoinduced charge carriers. Time-resolved photoluminescence analysis further elucidates dynamic charge transfer processes. As shown in Fig. 6c, the lifetime of photoexcited electrons in PtCu/Ti-$H_2$ is significantly prolonged, attributed to defect states in PtCu/Ti-$H_2$ that hinder electron–hole recombination. This finding is consistent with the photocurrent response and EIS results. UV–vis diffuse reflectance spectra were collected to assess the light absorption capacity of the various catalysts. Fig. 6d shows that PtCu/Ti-$H_2$ exhibits significantly increased intensity in the visible light region, indicating enhanced responsiveness to visible light. This enhancement is attributed to the $Pt^{\delta+}$-Ov-$Ti^{3+}$ and $Cu^{\delta+}$-Ov-$Ti^{3+}$ structures, which introduce tail states in the bandgap and broaden the absorption spectrum. The band gap of a photocatalyst determines its light response range. A larger band gap typically corresponds to shorter wavelengths (UV light), limiting the catalyst's light response range. Conversely, a smaller band gap allows for the absorption of a broader spectrum, including more visible light, thereby improving light utilization efficiency. The band gaps of the photocatalysts were calculated using the formula $(\alpha h\nu)^{1/n} = A(h\nu - E_g)$. As shown in Fig. S25, the calculated band gap order was as follows: Ti > Ti-$H_2$ > PtCu/Ti > PtCu/Ti-$H_2$. Consequently, PtCu/Ti-$H_2$ exhibits a wider light response range, contributing to a higher $CH_4$ yield, consistent with previous studies (Guan et al., 2024). These photoelectrical properties align well with the catalytic activity results, indicating that the electrons from Pt and Cu atoms transfer to Ti via the Ovs at the $Pt^{\delta+}$-Ov-$Ti^{3+}$ and $Cu^{\delta+}$-Ov-$Ti^{3+}$ interface in the PtCuTi-$H_2$ catalyst, thereby enhancing its photocatalytic $CO_2$ reduction activity.

To identify the surface active sites for $CO_2$ photoreduction, we conducted $CO_2$-TPD experiments. As shown in Fig. 7a, the Ti sample exhibited three desorption peaks: one for the physisorption of $CO_2$ (85 °C), another for carbonates at 353 °C, and a third for bicarbonates at 434 °C. After hydrogen reduction treatment, a new desorption peak appeared at 329 °C, attributed to $CO_2$ adsorbed at Ovs on the surface of Ti-$H_2$. Fresh samples with the deposited PtCu alloy exhibited an additional desorption peak at 258 °C, corresponding to $CO_2$ adsorbed on the PtCu alloy, as noted in previous reports (Wang et al., 2024a,b,c). Notably, PtCu/Ti-$H_2$ showed desorption peaks for $CO_2$ adsorbed at Ov (347 °C) and on the PtCu alloy (307 °C), as well as an additional desorption peak at 387 °C, which is assigned to $CO_2$ adsorbed at $Pt^{\delta+}$-Ov-$Ti^{3+}$ and $Cu^{\delta+}$-Ov-$Ti^{3+}$ sites. The higher desorption temperature of this peak indicates stronger $CO_2$ adsorption at the interface, facilitating the hydrogenation reaction, consistent with previous findings (Liang et al., 2018). Combining the results from Raman spectra, XPS, and EPR, we conclude that the interaction between PtCu and $TiO_2$ leads to the formation of $Pt^{\delta+}$-Ov-$Ti^{3+}$ and $Cu^{\delta+}$-Ov-$Ti^{3+}$ species at the interface. This interaction likely enhances $CO_2$ adsorption activation on PtCu/Ti-$H_2$.

To further investigate the enhanced $CH_4$ production on the PtCu/Ti-$H_2$ catalyst, *in situ* DRIFTS was conducted during the photocatalytic $CO_2$ reduction reaction, as shown in Fig. 7. After saturating the system with $H_2O$ and $CO_2$, the catalysts were irradiated with a 300-W xenon lamp. As illustrated in Fig. 7b and c, bands attributed to $*CO_2$ and physisorbed $H_2O$ on the PtCu alloy were detected at 1677 $cm^{-1}$ and 1649 $cm^{-1}$ for both PtCu/Ti and PtCu/Ti-$H_2$ catalysts (Wang et al., 2024a,b,c). Notably, PtCu/Ti-$H_2$ exhibited a significantly more intense $*CO_2$ band compared to PtCu/Ti, suggesting that the $Cu^{\delta+}$-$Pt^{\delta+}$ sites are more favorable for $CO_2$ adsorption (Yu et al., 2021). Additionally, the PtCu/Ti-$H_2$ catalyst displayed a markedly intensified band at 1649 $cm^{-1}$ associated with physisorbed $H_2O$, indicating a higher affinity for $H_2O$ adsorption, corroborated by the smaller contact angle observed on the surface of PtCu/Ti-$H_2$ (Fig. S27). Another band detected at 1373 $cm^{-1}$ was assigned to $*CO_3^{2-}$, suggesting $CO_2$ adsorption on the $Pt^{\delta+}$-Ov-$Ti^{3+}$ and $Cu^{\delta+}$-Ov-$Ti^{3+}$ interface structure (Yu et al., 2021). After 12 min of illumination, new bands at 1725 $cm^{-1}$ and 1571 $cm^{-1}$ appeared in the *in situ* DRIFTS spectra for both PtCu/Ti and PtCu/Ti-$H_2$, indicating the formation of *COOH intermediates (Fu et al., 2020). Importantly, PtCu/Ti-$H_2$ also showed two new bands at 1422 $cm^{-1}$ and 1161 $cm^{-1}$ attributed to $*HCO_3^-$ and *COOH species, indicating the hydrogenation of $CO_2$ at the $Pt^{\delta+}$-Ov-$Ti^{3+}$ and $Cu^{\delta+}$-Ov-$Ti^{3+}$ interfaces (Neaţu et al., 2014). Subsequently, a band assigned to *CO appeared near 1361 $cm^{-1}$, followed by bands at 1610 $cm^{-1}$ and 1508 $cm^{-1}$ corresponding to *CHO and $*CH_2O$ intermediates, respectively (Yin et al., 2022). With further illumination, bands attributed to $*CH_3O$ appeared at 1128 $cm^{-1}$ and 1463 $cm^{-1}$ (Wang et al., 2023a,b). Interestingly, the intensities of the bands corresponding to *COOH, *CO, *CHO, and $*CH_2O$ intermediates on the PtCu/Ti-$H_2$ catalyst were weaker compared to those on PtCu/Ti, indicating a faster consumption of these intermediates due to their adsorption at the $Pt^{\delta+}$-Ov-$Ti^{3+}$ and $Cu^{\delta+}$-Ov-$Ti^{3+}$ interfaces. Based on the observed intermediates, we propose the following reaction mechanism: $*CO_2 \rightarrow *COOH \rightarrow *CO \rightarrow *CHO \rightarrow *CH_2O \rightarrow *CH_3O \rightarrow CH_4 + *O \rightarrow CH_4 + *OH \rightarrow CH_4 + H_2O$. This suggests that the PtCu/Ti-$H_2$ catalyst exhibited an enhanced formaldehyde mechanism.

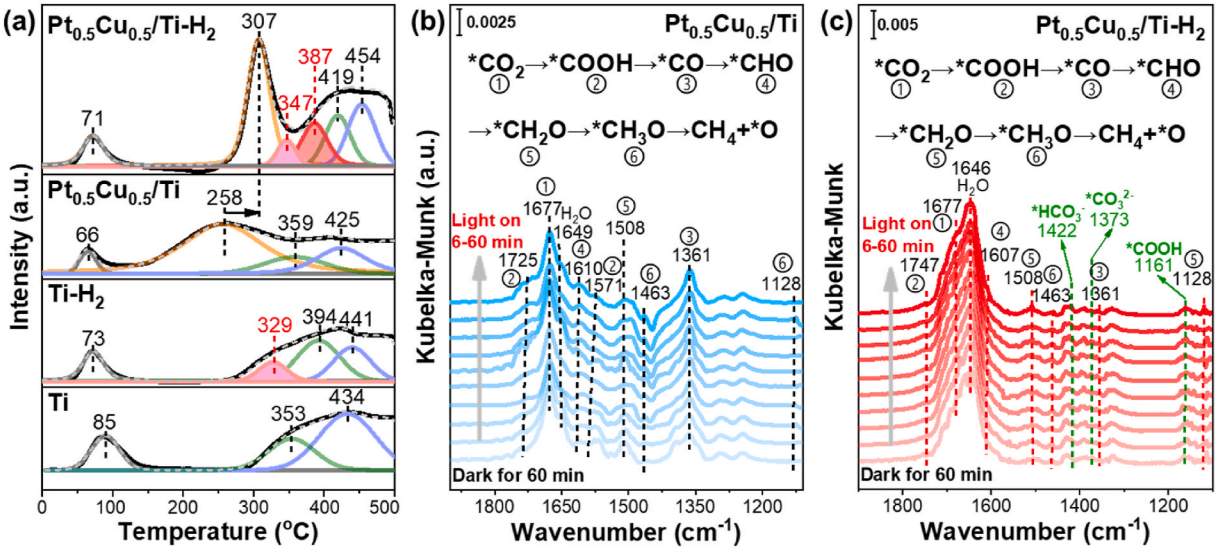


**Fig. 7.** Adsorption and reaction mechanism; (a) $CO_2$-TPD profiles of fresh Ti, pretreated Ti-$H_2$, fresh PtCu/Ti, and pretreated PtCu/Ti-$H_2$ catalysts; *in situ* DRIFTS of the reaction between $CO_2$ and $H_2O$ on fresh PtCu/Ti (b) and pretreated PtCu/Ti-$H_2$ (c).

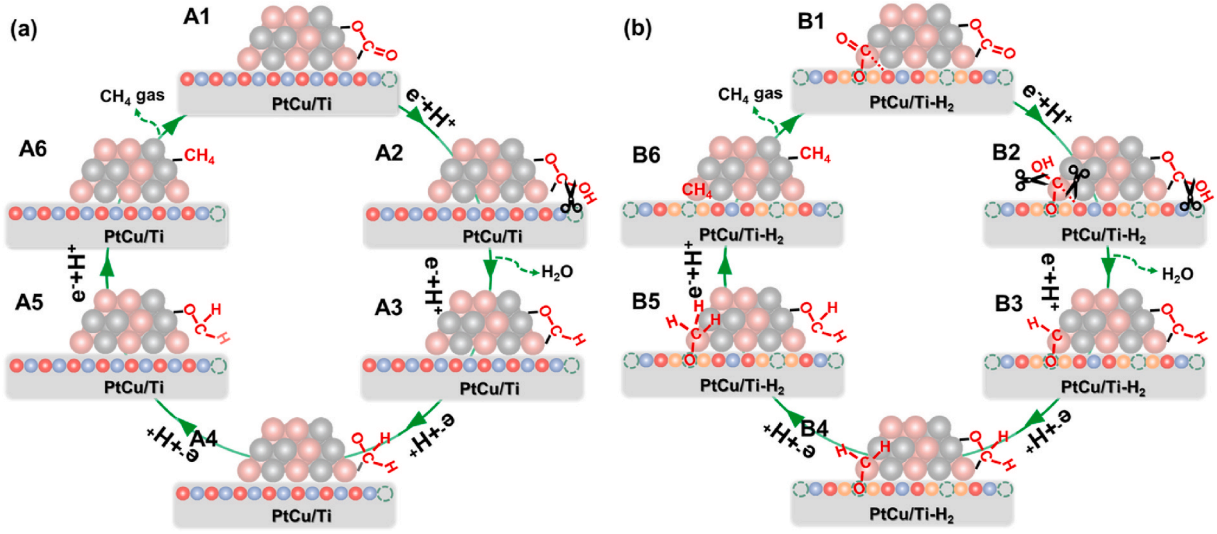


**Fig. 8.** Proposed reaction mechanisms for PtCu/Ti (a) and PtCu/Ti-$H_2$ (b).

Combining the results from $CO_2$-TPD, EPR, and *in situ* DRIFTS, we propose the reaction mechanisms PtCu/Ti and PtCu/Ti-$H_2$ catalysts. Fig. 8 illustrates the reaction pathways for both catalysts. For PtCu/Ti (Fig. 8a), the reduction of $CO_2$ begins with the adsorption of carbon and oxygen atoms from the $CO_2$ molecule onto adjacent Cu-Pt atomic pairs (A1), specifically on the Cu and Pt atoms. These adsorbed atoms then receive electrons and combine with dissociated $H^+$ from $H_2O$ to form *COOH (A2). Another $H^+$ from $H_2O$ attacks the OH of *COOH, resulting in the formation of $H_2O$ molecule that desorbs from the surface, leaving *CO (A3). The *CO subsequently receives an electron and combines with a third hydrogen to generate *CHO (A4). Finally, *CHO undergoes three electron transfers combined with dissociated $H^+$ to produce $CH_4$ (A7). For the PtCu/Ti-$H_2$ catalyst, the reaction pathway begins similarly to that of the PtCu/Ti catalyst, with $CO_2$ adsorption on the PtCu alloy. A notable distinction is the adsorption of an oxygen atom from the $CO_2$ molecule onto an interfacial Ov, leading to the formation of negatively charged $*CO_3^{2-}$ (B1) (Fig. 8b). This negatively charged $*CO_3^{2-}$ at the interfacial Ov then forms $*HCO_3^-$ (B2). Following this, the enhanced hydrogenation steps described previously occur while the oxygen atom of $CO_2$ remains adsorbed at the interfacial Ov. This observation sheds light on the differences in catalytic activity between the PtCu/Ti and PtCu/Ti-$H_2$ catalysts.

## 4. Conclusion

Through a simple hydrogen reduction treatment, we successfully manipulated the interface structure of the fresh PtCu/Ti catalyst, resulting in the formation of abundant $Pt^{\delta+}$-Ov-$Ti^{3+}$ and $Cu^{\delta+}$-Ov-$Ti^{3+}$ species at the interface. This modification facilitates electron transfer from Pt and Cu to Ti via the Ovs within the interface structure. Comprehensive characterizations revealed that these $Pt^{\delta+}$-Ov-$Ti^{3+}$ and $Cu^{\delta+}$-Ov-$Ti^{3+}$ interface structures serve as effective $CO_2$ adsorption and activation, enhance the visible light absorption range, and improve charge carrier separation. Mechanistic investigations demonstrated that the $Pt^{\delta+}$-Ov-$Ti^{3+}$ and $Cu^{\delta+}$-Ov-$Ti^{3+}$ interface structures in PtCu/Ti-$H_2$ promote the consumption of reaction intermediates and facilitate their conversion to gaseous $CH_4$. This enhancement resulted in $CH_4$ production rates approximately 2 times and 81.6 times higher than those of the fresh PtCu/Ti catalyst and benchmark anatase $TiO_2$, respectively. This study not only provides an atomic-level understanding of how catalytic activity depends on the PtCu/$TiO_2$ interface structure but also offers a strategic approach for designing alloy/oxide interfaces to optimize heterogeneous catalysis for photocatalytic $CO_2$ reduction. This opens up new possibilities for increased $CH_4$ production. For practical industrial applications of the PtCu/Ti-$H_2$ catalyst, future research should focus on reducing the cost and further enhancing the catalyst's stability under industrial reaction conditions.

## CRediT authorship contribution statement

**Xin Wang:** Writing – original draft, Conceptualization. **Wei Tan:** Conceptualization. **Bo Peng:** Conceptualization. **Shangcong Sun:** Conceptualization. **Xue Li:** Methodology. **Kaiqiang Wang:** Methodology. **Jiawei Ji:** Methodology. **Haohong Liao:** Methodology. **Jingfang Sun:** Conceptualization. **Qing Tong:** Conceptualization. **Haiqin Wan:** Conceptualization. **Lin Dong:** Writing – review & editing, Conceptualization.

## Declaration of competing interest

The authors declare that they have no known competing financial interests or personal relationships that could have appeared to influence the work reported in this paper.

## Acknowledgment

This work was supported by the State Key Laboratory of Catalytic Materials and Reaction Engineering (RIPP, SINOPEC), the Natural Science Foundation of Jiangsu Province (BK20231513) and the National Natural Science Foundation of China (No. 22106067 and 22272077).

## Appendix A. Supplementary data

Supplementary data to this article can be found online at https://doi.org/10.1016/j.envres.2024.120191.

## Data availability

Data will be made available on request.

## References

Chen, J.J., et al., 2020. General synthesis of ultrafine Cu-based alloy nanoparticles anchored on porous N-doped carbon nanofibers for enhanced electrocatalytic performance. J. Phys. Chem. C 124, 13036–13044.
Di, J., et al., 2024. Asymmetric electron redistribution in niobic-oxygen vacancy associates to tune noncovalent interaction in $CO_2$ photoreduction. Adv. Mater. 36, 2401914.

Dong, F., et al., 2024. Atomic Pt sites anchored in the interface between grains on vacancy-enriched $CeO_2$ nanosheets: one-step precursor combustion synthesis. Adv. Mater. 36, 2401055.
Du, C., et al., 2024. Boosting exciton dissociation and charge transfer in $CsPbBr_3$ QDs via ferrocene derivative ligation for $CO_2$ photoreduction. Proc. Natl. Acad. Sci. USA 121, e2315956121.
Fang, F., et al., 2024. Ordering bimetallic Cu-Pd catalysts onto orderly mesoporous $SrTiO_3$-crystal nanotubular networks for efficient carbon dioxide photoreduction. Angew. Chem. Int. Ed. 63, e202405807.
Fu, J., et al., 2020. Product selectivity of photocatalytic $CO_2$ reduction reactions. Mater. Today 32, 222–243.
Gao, Y., et al., 2024. Construction of dual active sites in perovskite oxide for targeted photocatalytic $CO_2$ reduction to $CH_4$. ACS Catal. 14, 10746–10759.
Guan, Q., et al., 2024. Non-metal sulfur doping of indium hydroxide nanocube for selectively photocatalytic reduction of $CO_2$ to $CH_4$: a "one stone three birds" strategy. Adv. Sci. 11, 2401990.
He, Y., et al., 2023. Interfacial effects promote the catalytic performance of $CuCoO_2$-$CeO_2$ metal oxides for the selective reduction of NO by CO. Chem. Eng. J. 465, 142856.
Howe, R.F., Gratzel, M., 1985. EPR observation of trapped electrons in colloidal titanium dioxide. J. Phys. Chem. 89, 4495–4499.
Imai, K., et al., 2024. Visible-light responsive $TiO_2$ for the complete photocatalytic decomposition of volatile organic compounds (VOCs) and its efficient acceleration by thermal energy. Appl. Catal., B: Environment and Energy 346, 123745.
Janotti, A., et al., 2010. Hybrid functional studies of the oxygen vacancy in $TiO_2$. Phys. Rev. B 81, 085212.
Khan, M.S., et al., 2023. A review of metal–organic framework (MOF) materials as an effective photocatalyst for degradation of organic pollutants. Nanoscale Adv. 5, 6318–6348.
Kruk, M., Jaroniec, M., 2001. Gas adsorption characterization of ordered Organic−Inorganic nanocomposite materials. Chem. Mater. 13, 3169–3183.
Lee, S., et al., 2016. Low-coordinated surface atoms of CuPt alloy cocatalysts on $TiO_2$ for enhanced photocatalytic conversion of $CO_2$. Nanoscale 8, 10043–10048.
Li, C., et al., 2023. Improving oxygen reduction performance of surface-layer-controlled Pt–Ni nano-octahedra via gaseous etching. Nano Lett. 23, 3476–3483.
Liang, L., et al., 2018. Infrared light-driven $CO_2$ overall splitting at room temperature. Joule 2, 1004–1016.
Liu, S., et al., 2021. Encapsulation of platinum by titania under an oxidative atmosphere: contrary to classical strong metal–support interactions. ACS Catal. 11, 6081–6090.
Liu, S., et al., 2024. Particle size-dependent charge transfer dynamics for boosting $CO_2$ photoreduction over Ag/$TiO_2$ heterojunction. ACS Catal. 14, 8105–8115.
Nakamura, I., et al., 2011. Active sites for hydrogen dissociation over $TiO_x$/Au(111) surfaces. J. Phys. Chem. C 115, 16074–16080.
Neaţu, Ş., et al., 2014. Gold–copper nanoalloys supported on $TiO_2$ as photocatalysts for $CO_2$ reduction by water. J. Am. Chem. Soc. 136, 15969–15976.
Putri, D.I.M., et al., 2024. Removal of Cd(II) from aqueous solution using biosorbent based on agricultural waste sorgum bagasse (Sorghum bicolor (L.) Moench) activated NaOH. Chem. Ecol. 1–27.
Ruiz Santoyo, V., et al., 2021. Photocatalytic degradation of rhodamine B and methylene orange using $TiO_2$-$ZrO_2$ as nanocomposite. Catalysts 11, 1035.
Shen, M., et al., 2021. A Ti-OH bond breaking route for creating oxygen vacancy in titania towards efficient $CO_2$ photoreduction. Chem. Eng. J. 425, 131513.
Tang, Z., et al., 2022. Ternary heterojunction in rGO-coated Ag/$Cu_2O$ catalysts for boosting selective photocatalytic $CO_2$ reduction into $CH_4$. Appl. Catal. B Environ. 311, 121371.
Wang, H., et al., 2023a. Construction of $Pt^{\delta+}$–O(H)–$Ti^{3+}$ species for efficient catalytic production of hydrogen. ACS Catal. 13, 10500–10510.
Wang, J., et al., 2022a. PtCu alloy cocatalysts for efficient photocatalytic $CO_2$ reduction into $CH_4$ with 100% selectivity. Catal. Sci. Technol. 12, 3454–3463.
Wang, K., et al., 2023b. Metallic $AgInS_2$ nanocrystals with sulfur vacancies boost atmospheric $CO_2$ photoreduction under near-infrared light illumination. Appl. Catal. B Environ. 332.
Wang, L., et al., 2021. A facile synthesis of brown anatase $TiO_2$ rich in oxygen vacancies and its visible light photocatalytic property. Solid State Ionics 361, 115564.
Wang, W., et al., 2024a. Enrooted-type metal-support interaction boosting oxygen evolution reaction in acidic media. Angew. Chem. Int. Ed. 63, e202406947.
Wang, X., et al., 2024b. Surface coordination environment engineering on $Pt_xCu_{1-x}$ alloy catalysts for the efficient photocatalytic reduction of $CO_2$ to $CH_4$. ACS Appl. Mater. Interfaces 16, 22089–22101.
Wang, Y., et al., 2022b. Insight on reaction pathways of photocatalytic $CO_2$ conversion. ACS Catal. 12, 7300–7316.
Wang, Z., et al., 2024c. Localized surface plasmon resonance-induced bidirectional electron transfer of formic acid adsorption for boosting photocatalytic hydrogen production on Ni/$TiO_2$. Chem. Eng. J. 482, 148942.
Xie, B., et al., 2024a. Enhanced Ru-O-Ce interaction by solid solution structure of Ru-$Ce_xZr_{1-x}O_2$ catalysts for efficient catalytic combustion of vinyl chloride. Appl. Catal., B: Environment and Energy 350, 123926.
Xie, Z., et al., 2024b. Clustering-resistant Cu single atoms on porous Au nanoparticles supported by $TiO_2$ for sustainable photoconversion of $CO_2$ into $CH_4$. Angew. Chem. Int. Ed., e202410250 n/a.
Xu, L., et al., 2016. Plasma-engraved $Co_3O_4$ nanosheets with oxygen vacancies and high surface area for the oxygen evolution reaction. Angew. Chem. 128, 5363–5367.
Yin, H., et al., 2022. Coupling Cu single atoms and phase junction for photocatalytic $CO_2$ reduction with 100% CO selectivity. ACS Catal. 12, 14096–14105.
Yoshino, S., et al., 2022. $CO_2$ reduction using water as an electron donor over heterogeneous photocatalysts aiming at artificial photosynthesis. Accounts Chem. Res. 55, 966–977.
Yu, J., et al., 2023. Artificial spherical chromatophore nanomicelles for selective $CO_2$ reduction in water. Nat. Catal. 6, 464–475.
Yu, S.-W., et al., 2024. Construction of a Pt-$CeO_x$ interface for the electrocatalytic hydrogen evolution reaction. Adv. Funct. Mater. 63, 2402966.
Yu, Y., et al., 2021. Synergistic effect of Cu single atoms and Au–Cu alloy nanoparticles on $TiO_2$ for efficient $CO_2$ photoreduction. ACS Nano 15, 14453–14464.
Zhou, Y., et al., 2016. Interplay of Pt and crystal facets of $TiO_2$: CO oxidation activity and operando XAS/DRIFTS studies. ACS Catal. 6, 7799–7809.